Influence of low level of non-metal doping on g-C3N4 performance for H2 production from water under solar light irradiation

Leila Hammoud, Clément Marchal, Valérie Caps, Joumana Toufaily, Tayssir Hamieh, Valérie Keller

Influence of low level of non-metal doping on g-C_3N_4 performance for H_2 production from water under solar light irradiation

Leila Hammoud,[a,b] Clément Marchal,[a] Valérie Caps,[a] Joumana Toufaily,[b] Tayssir Hamieh,[b] Valérie Keller[a]

[a] *ICPEES, Institute of Chemistry and Processes for Energy, Environment and Health, UMR 7515 CNRS/University of Strasbourg, 25 rue Becquerel, 67087, Strasbourg, cedex 2, France*
[b] *MCEMA, Laboratory of Materials, Catalysis, Environment and Analytical Methods, Lebanese University, Hadath, Campus Rafic Hariri, Beyrouth, Lebanon*

* Corresponding author.
E-mail address: vkeller@unistra.fr (V. Keller).

Highlights

- H_2 production by water splitting with non-metal doped g-C_3N_4 using low amount (1 vol%)TEOA.
- Enhanced H_2 production rate induced by trace level (<0.1 wt%) of S-dopant.
- Benefits of low-level doping strategy to overcome the main limitations of g-C_3N_4.
- One-pot easy synthesis of nonmetal doping of g-C_3N_4 during thermal polycondensation.
- Those photocatalyst exhibit enhanced visible light harvesting properties.

Keywords: g-C_3N_4, hydrogen, Non-metal doping, Water-splitting, Photocatalysis

Graphical abstract

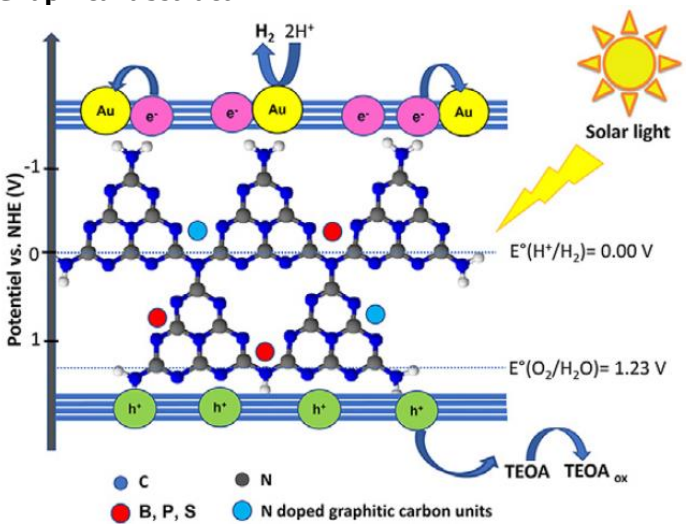

Abstract

In this paper, a facile one step synthesis method for the preparation of C-, B-, P- and S-doped g-C_3N_4 by incorporation of small concentration of doping element precursor into urea during thermal polycondensation is reported leading to much lower doping levels than the ones usually reported. The as-obtained doped g-C_3N_4 photocatalytic materials are deeply characterized in terms of structural, morphological, surface and optical properties. Doping yields beneficial surface morphology modulation along with improved optical, electronic and photocatalytic properties. In particular, C-doped and S-doped g-C_3N_4 show, after deposition of gold nanoparticles (<1 wt%), enhanced photocatalytic performance (at least twice as high as the undoped photocatalyst, to achieve ca. 610 µmol/h/g) for the production of H_2 by water splitting under solar light in the presence of low content (1 vol%) of triethanolamine (TEOA) as sacrificial agent. The most remarkable activity results from the incorporation

of traces of S dopant, mainly inserted into interplanar hollow cavities. The enhanced activity is attributed to a combination of high surface area, location of the S dopant and small size of the co-catalyst NPs, which induces enhanced visible light harvesting, enhanced charge carrier separation and enhanced proton recombination. This work highlights the benefits of the optimized low-level doping strategy to overcome the main limitations of g-C_3N_4-based photocatalysts.

Introduction

Growing global energy depletion and worsening environmental pollution from the depletion of non-renewable sources has sparked intensive research interest around the world since the 1970s [1,2]. Replacing these fossil fuels with clean renewable energies is one of the challenges currently being researched [3]. Among the different types of renewable energy available, solar energy is the most abundant source of energy arriving on earth. Yet it is very little used and accounts for only 2% of the world's electricity production [4]. The development of new technologies allowing the storage of solar energy in another form of energy is a very important task. Among the wide variety of processes discovered, semiconductor-based photocatalysis has become one of the promising technologies, allowing the conversion of solar energy into chemical energy in the form of a transportable, storable and useable energy carrier [5,6]. In 1972, Fujishima and Honda were the first to produce H_2 from water splitting using an n-TiO_2 cell attached to Pt [7]. Thus, the search for abundant, inexpensive and robust semiconductors with high catalytic activity under visible light is in great demand to meet the needs of terawatt energy transfer.

Graphitic carbon nitride has been of interest since Wang et al. first discovered its ability for photocatalytic H_2 and O_2 evolution in 2009 [8]. It is a metal free polymer n-type semiconductor, possessing many interesting properties, such as high thermal, physical, chemical and photochemical stability, which make g-C_3N_4-based materials a new class of multifunctional nanoplatforms for solar water splitting [9,10], pollutants photodegradation [11-13], carbon dioxide reduction [14], etc. g-C_3N_4 has an optical band-gap (≈ 2,7 eV) corresponding to a wavelength of ca. 460 nm [15], which makes it active under visible light. It is considered as an organic semiconductor mainly composed of carbon and nitrogen, which are among the most abundant elements on the Earth [16]. It can be synthesized at low cost by pyrolysis of nitrogenrich precursors like urea, thiourea, cyanamide, dicyandiamide, melamine [8,17,18], etc. However, the texture, electronic structure and performance of g-C_3N_4 are strongly dependent on the type of precursor used, due to the different formation processes and degrees of condensation involved [19]. Recently, urea has emerged as an inexpensive nitrogen precursor suitable for large-scale production. It is the only nitrogen precursor which leads, without structuring agent, to the synthesis of highly porous g-C_3N_4 with large specific surface areas and therefore a potentially high photocatalytic activity [17].

However, g-C_3N_4 suffers from certain limitations such as rapid recombination between photogenerated electron/hole pairs and limited absorption of visible light [20]. Several approaches can be used to improve the photocatalytic performances of g-C_3N_4, including nanostructuring [21,22], doping by metals and non-metals [15,23,24], exfoliation [25], controlling morphologies and geometric shapes [26], and copolymerization [27]. Doping of graphitic carbon nitride with nonmetal element in particular modulates its surface morphology, electronic structure, size of particles, optical and physicochemical properties [15]. This non-metal incorporation generally allows to tune the band structure, extend absorption of visible irradiation and create more active sites [28].

Self-doping C_3N_4 with carbon has been pointed out as an efficient strategy to change the surface and electronic properties of g-C_3N_4 without introducing other foreign atoms and defects [29], and to obtain enhanced visible light absorption, better separation of photo-excited charge carriers thanks to better π-electrons delocalization [30], and a negative shift in the CB edge potential [31].

B-doping of C_3N_4 allows to tune magnetic and electronic properties of carbon nitride [32,33] and can be used for visible lighteddriven photocatalysis [34,35]. B-doped C_3N_4 can be obtained by heating a mixture of melamine and boron oxide in N_2 atmosphere [36] or by a one-step calcination of 4- pyridylboronic acid as both a boron and a nitrogen source [37]. In some materials, it has been shown that functional groups with a B-C bond can act as Lewis acid sites. The doping of g-C_3N_4 by phosphorus can regulate the band gap structure and improve the carrier separation efficiency. P-doped g-C_3N_4 can be prepared via thermal condensation of adenosine phosphate and urea followed by thermal exfoliation method [38] or via thermal copolymerization of hexachlorocyclotriphosphazene as phosphorus source and

guanidiniumhydrochloride as g-C_3N_4 precursor, and exhibit excellent photocatalytic performance both in the photoconversion of H_2O to produce H_2 and the photodegradation of Rhodamine B (RhB) [39]. P-doped tubular g-C_3N_4 with surface defects have been obtained from a supramolecular precursor under sodium pyrophosphate assisted hydrothermal synthesis, showing excellent photocatalytic production of hydrogen under visible light [40].

Sulfur atom doping has been utilized to optimize the electronic band structure of g-C_3N_4. It can be achieved by thermal treatment under H_2S [41], thermal polymerization or copolymerization with S-containing compounds [42,43], and by sulfuring g-C_3N_4 [44]. For example, sulfur-doped terminal methylated g-C_3N_4 nanosheets with a tunable band gap were obtained by thermal copolymerization of thioacetamide as a sulfur source and blocking agent [45]. Sulfur-doped twodimensional graphitic carbon nitride nanosheets with high surface area and efficient activity in photocatalytic watersplitting were synthesized via polycondensation of thiourea followed by thermal oxidative etching treatment of the obtained S-g-C_3N_4 [46].

Here we report a facile one step synthesis method for the preparation of C-, B-, P- and S-doped g-C_3N_4 with low dopant content. The as-obtained photocatalysts exhibit decreased band gap energies, which leads to increased visible light absorption properties and better charge carrier separation, while maintaining high surface area. It is shown that, after addition of gold nanoparticles, S-doped graphitic carbon nitride at sulfur trace level can effectively enhance the photocatalytic performances for the production of H_2 by water splitting under solar light in the presence of triethanolamine (TEOA, 1 vol%) as sacrificial agent. Extensive characterization of the structural, morphological, surface and optical properties show that Au/CN-S combines a low stacking degree, high surface area, large mesoporosity, small Au NPs size and narrow Au NP size distribution, which is beneficial to the photocatalytic reaction.

Experimental

Materials

Urea (NH_2CONH_2, 99%, Sigma Aldrich), citric acid monohydrate ($HOC(COOH)CH_2COOH)_2.H_2O$, ≥99%, Sigma Aldrich), boric acid (H_3BO_3, ≥99,5%, Sigma Aldrich), sodium phosphate monobasic (NaH_2PO_4, ≥99%, Sigma Aldrich), chloroauric acid ($HAu^{III}Cl_4.3H_2O$)(≥99,9% trace metal basis, Alfa Aesar), sodium borohydride (≥98%, Sigma Aldrich), ethanol (CH_3CH_2OH, ≥96%, Sigma Aldrich), triethanolamine (TEOA, ≥99%, Sigma Aldrich), 2-thiobarbituric acid ($C_4H_4N_2O_2S$, ≥98%, Sigma Aldrich) were used without further purification.

Pure g-C_3N_4 was synthesized via thermal polycondensation of urea at 550 °C for 3 h, with a heating ramp rate of 15 °C/min. 10 g of urea was put into an aluminum crucible with a top cover. The obtained product is denoted as CN. The non-metal element doped g-C_3N_4 were synthesized by mixing urea (10 g) and 10 mg of the precursor of non-metal elements (H_3BO_3 for element B, NaH_2PO_4 for element P, $HOC(COOH)CH_2COOH)_2.H_2O$ (acetic acid) for element C and $C_4H_4N_2O_2S$ (2-thiobarbituric acid) for element S). After grinding, the mixture was annealed at 550 °C for 3 h in a muffle furnace with a heating ramp rate of 15 °C/min. The composites were named as CN-X, where X is the dopant element (C, B, P or S) in g-C_3N_4.

Au (0.86 wt % theoretical value) was loaded as a co-catalyst onto the surface of g-C_3N_4 by an impregnation-reduction method using chloroauric acid as the precursor of gold. In a 100 mL flask, 40 mL of H_2O, 80 mL of $HAu^{III}Cl_4.3H_2O$ (0.22 M in water) and 400 mg of C_3N_4 were mixed. The mixture is left under magnetic stirring (1000 rpm) for 45 min while the precursor is impregnated. Then 1 mL of a solution of $NaBH_4$ (0.1 M) was added (with $NaBH_4$/Au = 5) to the freshly prepared mixture. A grey coloration which highlights the reduction of the gold precursor and the formation of Au nanoparticles is observed. After the reduction, the mixture is stirred for 15 min and then the obtained material is filtered and washed with 1 L of distilled water. During filtration, the filtrate appears clear and colorless, which suggests that a good deposit has been obtained. Finally, the composite is placed in an oven at 100 °C for 24 h, and a grey powder of Au/g-C_3N_4 is obtained. The same deposition method was applied to the different doped-C_3N_4. By ICP-AES analysis, it was confirmed that the gold contents were all in the range 0.71-0.79 wt %, i.e. an average gold content of 0.75 ± 0.04 wt % and average deposition yield of Au nanoparticles on C_3N_4 of 87%.

The resulting samples are named CN for bare g-C_3N_4, CN-X for the doped-C_3N_4 samples (with X ¼ C, B, P or S) and Au/CN-X after Au deposition.

Materials characterization

The X-ray diffraction apparatus used is a Bruker D8 Advance diffractometer equipped with a Lynxeye XE detector operating at 40 kV and 40 mA in θ/θ mode. The source of the X-Rays is a copper anticathode using the Kα line at 1.5418 Å. In order to obtain normalized diffractograms, a fixed amount of the sample (50 mg) was placed on a plastic holder. The acquisition of diffractograms was performed in scanning mode in of the range 2θ = 10-38° with a step of 0.041° and a counting time of 5 s per step. The mean crystal thickness is calculated from the Debye-Scherrer equation based on the full width at half maximum and the position of the most intense peak at 2θ = 27.3°. This peak also makes it possible to obtain the interreticular distance between two crystal planes using Bragg's law $2 \times d(hk1) \times \sin(\theta) = n \times \lambda$, where d(hk1) represents the interreticular distance between two crystalline planes, θ is the Bragg angle, n is the diffraction order and λ represents the wavelength of the radiation (Å). The average number of sheets can also be calculated from the crystal domains and the distance between sheets.

Fourier transform infrared spectra (FTIR) were collected from 525 to 4000 cm^{-1} with a Thermo Fisher Nicolet spectrometer S10. Due to the physisorbed CO_2, the characteristic doublet of the atmospheric CO_2 signal 2340/2360 cm^{-1} could not be completely removed from the spectra after background subtraction. FT-IR spectra after photocatalytic tests were recorded after recovering, filtration, washing and drying of the sample in an oven for 12 h.

Nitrogen adsorption-desorption isotherms were obtained using a Micromeritics Asap 2420 porosimeter. The analysis was carried out under atmospheric pressure at the nitrogen liquefaction temperature (-196 °C). The materials were degassed at 150 °C under primary vacuum for 8 h with a temperature rise of 10°Cmin^{-1} in order to desorb water and adsorbed molecules from their surfaces. The specific surfaces of the materials were calculated from the adsorption isotherm by the BET method. From the desorption, the pore size distribution can be calculated by the BJH method specifically for mesoporous solids.

Thermogravimetric analyzes were performed using a model Q 5000 IR apparatus from TA Instrument equipped with a sample changer and a microbalance with a sensitivity of around 0.1 μg. 3 mg of each sample was placed in a platinum crucible, then heated from room temperature to a temperature of 800 °C with a temperature rise ramp of 15 C min^{-1} under an air flow rate of 25 mL min^{-1}.

Elemental analyzes of the samples were performed by Inductively Coupled Plasma Atomic Emission Spectrometry (ICP-AES, Varian 720 ES).

High-resolution transmission electron microscopy was performed on a Jeol 2100F microscope equipped with a lanthanum hexaboride cathode (LaB6) operating at 200 kV. The device is coupled with an EDS KEVEX Deltapro Quantum spectrometer which measures the dissipative energy of X-rays (EDX). The sample was sonicated in ethanol and then a drop of the suspension was placed on a carbon membrane placed on a copper grid. HRTEM is used to determine the size of gold nanoparticles and consequently the distribution in size is obtained by measuring the particles size for more than 100 particles using the ImageJ software [W. Rasband, http://rsb.info.nih.gov/ij/].

UV-vis absorption spectra were recorded on a PerkinElmer 950 spectrophotometer fitted with a Labsphere RSA ASSY 100 nm integrating sphere. The spectra are acquired in reflection mode (diffuse reflectance). In order to determine the absorbance coefficient, the diffuse reflectance spectra were converted to Kubelka-Munk units via the equation: $F(R) = (1-R)^2/2R$. To obtain the band gap (Eg) of the semiconductor (SC), the Tauc equation $(F(R)*h\nu)^S = (h\nu - Eg)$ was used where h is the Planck constant, v is the frequency and S is a coefficient which is ½ in the case of an SC indirect gap and 2 in the case of a direct band gap SC (½ for g-C_3N_4).

X-ray photoelectron spectroscopy (XPS) measurements were performed on an ultra-high vacuum spectrometer (UHV) equipped with a VSW Class WA hemispherical electron analyzer. The X-ray source used is a double anode of aluminum Al Kα X-Ray (1486.6 eV) as incident radiation. General and high-resolution spectra were recorded in constant energy mode (100 and 20 eV respectively). In order to correct the shift in binding energy due to the electrostatic charge, the internal reference used is the C1s peak at 288.0 eV characteristic of hybridized C bonded to N atoms in the striazine structural units of g-C_3N_4 [47]. The background noise is subtracted according to the Shirley method. Photocatalytic tests The photocatalytic activities of Au/doped and non-doped g-C_3N_4 catalysts were studied under atmospheric pressure and at room temperature as a function of the amount of hydrogen produced from water. In a first step, 200 mg of the photocatalyst were dispersed in a quartz reactor containing 720 mL of Milli-Q water and 8 mL of TEOA as sacrificial agent under a flow of nitrogen flowing at 100 mLmin^{-}

[1] with mechanical stirring at 700 rpm. The device was equipped with a double-walled quartz tube containing a 150 W ceramic metal halid lamp simulating the solar spectrum (23.6 mW cm^{-2}) and a cooling system regulating the reaction mixture at 20 °C. The entire device is connected to a μGC R-3000 apparatus (SRA Instrument) controlled by a Soprane software for on-line analysis of the gases produced and equipped with thermal conductivity detectors (TCD). Before each test, the system is purged (for 1 h) with a flow of nitrogen (500 mL/min, Alphagaz 2, SMARTOP) in order to remove the residual oxygen in the reactor. After purging, the lamp is turned on and the photocatalytic test lasts 3 h. Stable H_2 production is considered to be the value after reaching a stable plateau. The hydrogen specific formation rate (expressed in μmol/h/g) is determined by the expression:

$$r_{H_2}\left(\mu mol.h^{-1}.g^{-1}\right) = \frac{ppm \times f}{V_{m_{H2,20°C}}} \times \frac{1}{m_{cat}}$$

where ppm is the concentration of H_2 as analyzed by the μGC apparatus, f is the nitrogen flow (100 cc/min) and $V_{mH2,20°C}$ is the molar volume of H_2 at 20 °C. In order to study the stability of the initial photocatalyst, recycling tests were carried out on the most performant photocatalyst. Note that after each washing cycle, there was a 5% mass loss that has to be taken into account for the calculation of the mass-specific hydrogen evolution rate.

Results and discussion

Structural characterization (XRD)

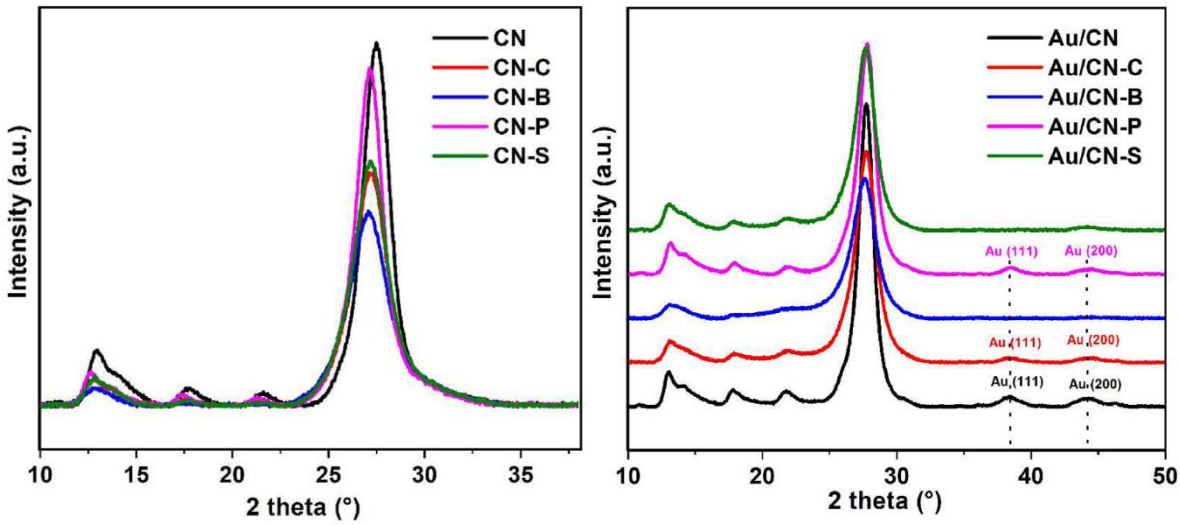

Fig. 1 *Normalized X-Ray diffraction pattern of (Top) Bare and doped-g-C_3N_4 and (Bottom) After Au (0.75 wt% nominal) deposition.*

The main X-ray diffraction peaks of undoped g-C_3N_4 (Fig. 1-Top) at 2θ = 13° and 2θ = 27.5° correspond respectively to the (100) plane of the in-plane structural packing and repeating motif of the heptazine (tri-s-triazine) network and to the interlayer stacking of π-conjugated aromatic systems, indexed as the (002) diffraction plane for graphitic materials [8]. The lower intensity diffraction peak at 17.5° can be attributed to the diffraction plane of the repeating motifs of the s-triazine unit of the aromatic system [48]. The calculated distance (Table 1), from the Bragg equation, corresponding to the size of the tri-s-triazine unit of g-C3N4 is 6.8 Å, slightly smaller than the theoretical size of ca. 7.3 Å. This difference could be attributed to the presence of small tilt angularity in the assembly, compared to theoretical assembly of tri-striazine units [45]. The calculated inter-planar distance between aromatic units of 3.24 Å is in good agreement with previous studies [8] and is related to a crystal thickness of 4.9 nm. From the Debye-Scherrer equation, it can be deduced that g-C_3N_4 is constituted of an average staking of 15 layers. XRD patterns of doped-g-C_3N_4 (Fig. 1-Top, Table 1) reveal a slight shift of the main diffraction

peaks towards lower angles, resulting in increasing both the tri-s-triazine repeating unit size and the interlayer distance. Nevertheless, the tri-striazine unit sizes remain smaller than the theoretical size (ca. 7.13 Å), probably due to small tilt angularity in the assembly as mentioned previously [45]. One can also mention (Table 1) that the mean stack thickness also decreases after doping, except for the P-doped C_3N_4 sample, leading to a decrease in the number of stacked layers. Amongst the different kinds of doping, it must be underlined that P-doping yields the largest heptazine repeating motif size and the most important crystallite thickness (and thus the largest number of layers) related to higher crystallinity. After Au deposition (Fig. 1-Bottom), new peaks appear in some of the diffractograms, at 38.2° and 44.3°, which can be attributed to the (111) and (200) reflections of gold, respectively (ICDD card No 00-004-0784). The absence of such peaks in the diffractograms of Au/CN-B and Au/CN-S, despite the similar gold content measured in all composites (Table 1), suggests that Au NPs are probably smaller in these two materials.

Looking at the N/C vol. ratio (Table 1), it must be mentioned that S- and C-doping yield a slight decrease compared to the other doped-materials and to bare g-C_3N_4, suggesting that C-slightly rich structure is obtained. One can also mention that the doping amounts remain lower than 1 wt% with traces doping level for S doping.

Table 1 – Tris-s-triazine unit distance, interlayer distance, crystallite thickness, number of stacked layers, doping element (N, C, B, P, S) and Au content (wt.%)*, N/C* volumic ratio. * Determined from ICP analyses.

	Tris-s-triazine d(Å)	d interlayer (Å)	Cryst. Thickn. (nm)	Nb. layers	N wt.%	C wt.%	N/C	B wt.%	P wt.%	S wt.%	Au wt.%
CN	6.80 ± 0.02	3.24 ± 0.01	4.9	15	59.25 ± 0.02	34.32 ± 0.02	1.73				0.77
CN –C	6.89 ± 0.02	3.28 ± 0.01	3.7	11	58.12 ± 0.02	33.92 ± 0.02	1.71				0.71
CN –B	6.85 ± 0.02	3.29 ± 0.01	3.4	10	56.75 ± 0.02	32.45 ± 0.02	1.75	0.87 ± 0.03			0.71
CN –P	6.97 ± 0.02	3.28 ± 0.01	4.8	15	58.45 ± 0,02	33.36 ± 0,02	1.75		0.70 ± 0.04		0.79
CN –S	6.88 ± 0.02	3.28 ± 0.01	3.7	11	58.52 ± 0,02	34.31 ± 0.02	1.71			0.03 ± 0.01	0.74

Thermal stability (TGA)

From TGA profiles of the undoped reference sample (Fig. 2), one can observe a one-pot decomposition profile in accordance with reported works [49,50], with decomposition starting at ca. 550 °C and with total decomposition achieved at 650 °C. Doping of g-C_3N_4 only leads to a slight shift to lower temperatures for the beginning of decomposition (ca. 530 °C), enhanced for B-doping for which the corresponding temperature is decreased to 460 °C. This feature is consistent with lower crystallite thickness and a lower number of stacked layers probably in weaker van der Waals interaction. Theoretically, thermal stability is correlated with ideal graphitic structure for g-C_3N_4. From TGA analyses showing only slight modifications of decomposition temperature, one can suggest that doping does not modify the main skeleton structure of g-C_3N_4.

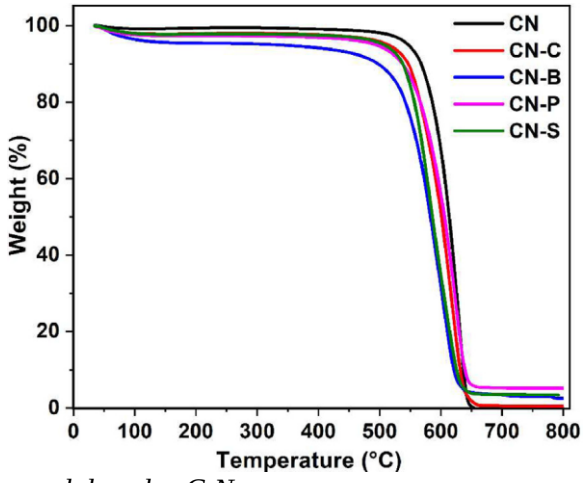

Fig. 2 *TGA analysis of bare and doped-g-C_3N_4*

Surface characterizations

FT-IR characterization

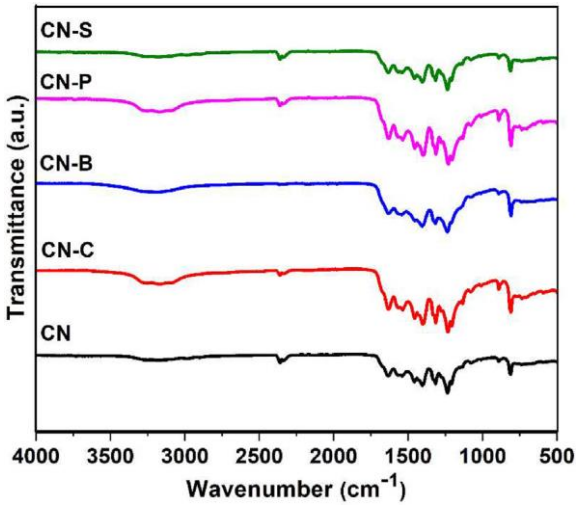

Fig. 3 *FT-IR spectra of undoped- and doped-g-C_3N_4.*

FT-IR spectra (Fig. 3) of all bare and doped g-C_3N_4 samples show the typical features of g-C_3N_4 materials in the 1240 to 1650 cm^{-1} region, assigned to the fingerprint of tri-s-triazine moieties vibration and characteristic of the presence of dimelem units [51,52]. More precisely, one can observe the specific bands at ca. 1630 and 1540 cm^{-1} corresponding to the asymmetric vibration of C-N bonds and at 1455, 1400, 1310 and 1230 cm^{-1} attributed to C-N stretching of secondary and tertiary aromatic amines. Furthermore, the absorption at ca. 800 cm^{-1} may be related to the tri-s-triazine breathing mode. From FT-IR characterization, it can be concluded that doping, and whatever the dopant element, does not noticeably impact the main and characteristic surface functions of g-C_3N_4 material and does not result in any additional vibrations related to in-plane stretching of newly formed bonds.

BET surface area and porosity measurements

From Fig. S1-Left, it can be observed that bare and doped gC_3N_4 exhibit type-IV adsorption-desorption isotherm profiles, which are characteristic of mesoporous/macroporous solids. The as-synthesized g-C_3N_4 samples all present a high surface area (Table 2) for this kind of materials. The highest surface area, reaching 170 m^2/g, is obtained for the bare g-C_3N_4. Doping leads to a decrease, which is more or less pronounced depending on the doping element and amount. The most important decrease (95 m^2/g) is observed after P-doping and the less marked one (136 m^2/g) after S-doping. It also appears from Fig. S1-Right and Table 2 that doping results in a decrease of the total pore volume, in line with the evolution of the surface areas. From Fig. S1-Right it can be seen that bare g-C_3N_4 is characterized by two kinds of pore structures, a main mesoporous/macroporous contribution centered at ca. 35 nm, that can be assigned to interplanar hollow space cavities, and a second and minor one at ca. 2-3 nm, probably linked to intra-planar space, keeping in mind the large uncertainty of micropores (<2 nm) distribution. One can observe that doping mainly leads to a shift of the meso/macroporosity contribution to larger pore diameters that may be correlated to the formation/presence of larger hollow space cavities, even if the total pore volume decreases. Furthermore, it is worthy to underline that S-doping, which consist in the lowest doping concentration (only 0.03 wt% of S, Table 1), yields specifically to the most important shift of the main pores size distribution towards higher values of ca. 50 nm, in line with the largest pore volume among the doped materials.

XPS characterization

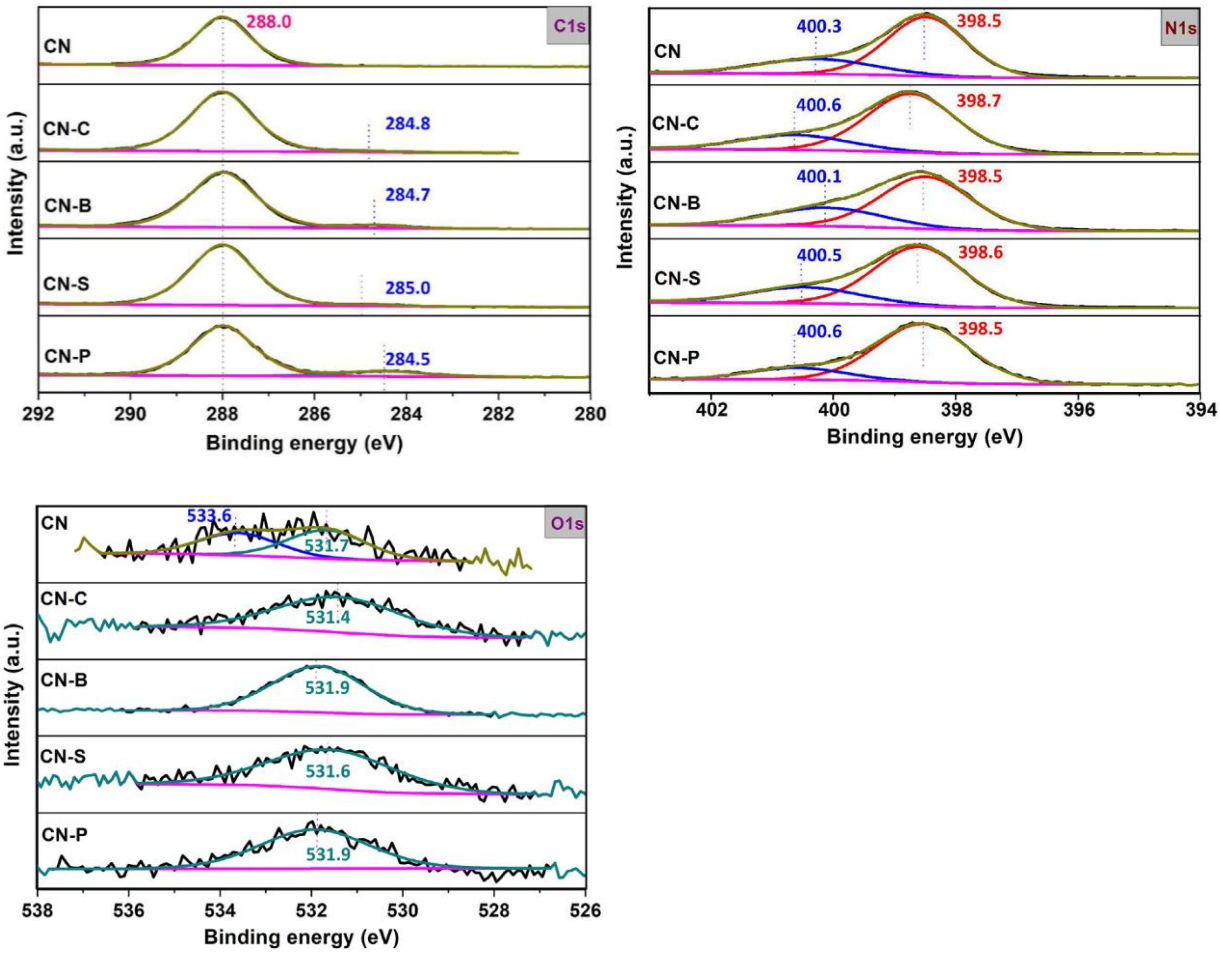

Fig. 4 *XPS spectra of bare and doped-gC_3N_4. (Top) C1s, (Middle) N1s and (Bottom) O1s.*

From XPS analysis of the C1s region (Fig. 4-Top), one can clearly observe the main contribution at 288.0 eV related to the typical feature of the sp^2-hybridized C bonded to N atoms units ($(N)_2$-C=N) of the aromatic skeleton of s-triazine rings (taken as the reference line for charging effect correction [52]. In addition, a second very low contribution at ca. 284.7-285.0 eV, not observed on bare g-C_3N_4, can be assigned to sp^2 graphitic C impurities.

N1s spectra (Fig. 4-Middle) reveal the two characteristic contributions in g-C_3N_4 materials with a first peak at 398.5 eV related to sp^2-hybridized N bonded to C atoms (C-N=C) in carbon-containing triazine ring (graphitic-N) and a second one at 400.3 eV attributed to bridging-N ternary atoms in N-$(C)_3$ group. It must be mentioned that this last contribution is shifted towards higher binding energy on C-, S- and P-doped g-C_3N_4 samples suggesting that these bridging-N atoms are in more pronounced electron-deficient configuration, compared to the undoped material. On the contrary on the B-doped sample, it is shifted towards lower binding energy, suggesting that the bridging-N atoms interact with electron donor species and that their electron density is increased. This important negative shift of bridging-N contribution on B-doped material may be explained according to the electronegativity order of B (2.0), P (2.2), C (2.5), S (2.6) and N (3.0). Furthermore, one can also underline that the graphitic-N/bridging-N ratio decreases after doping, except for B- and P-doping. This means that the content of bridging-N atoms is higher in C-doped and S-doped g-C_3N_4. Finally, one could not exclude a minor contribution at higher binding energy that could be assigned to amino groups, as already reported in some case in literature on doped graphitic carbon nitrides [28].

O1s spectra (Fig. 4-Bottom) present much lower intensities underlying low contributions of oxygen-containing groups onto g-C_3N_4 surfaces. O1s spectra can be decomposed into two main contributions on bare g-C_3N_4, the first one located at ca. 531.7 eV can be due to -OH surface groups and the second one at ca. 533.6 eV to adsorbed H_2O from atmosphere during preparation, as already reported [53]. One can noticed that doping leads to the absence of the second contribution. Furthermore, C-doping results

in a decrease in the binding energy corresponding to hydroxyl groups, whereas B-doping leads to an increase in this value. It must also be noted, looking at O/C atomic ratios, that B- and P-doped g-C_3N_4 exhibit slightly higher content of oxygen-containing species.

Table 3 – O1s and N1s contributions, C/N, O/C, Au/C, B/C, S/C and P/C surface atomic ratios (at.%) of bare and doped g-C_3N_4.

	O1s –OH	O1s –H_2O	N1s N–(C)$_3$	N1s (C–N=C)	Surface atomics ratios (at.%)						
					(C–N=C)/N–(C)$_3$	C/N	O/C	Au/C	B/C	S/C	P/C
CN	56.0	44.0	73.0	27.0	0.37	0.67	0.01				
CN–C	100	0	76.3	23.7	0.31	0.68	0.02				
CN–B	100	0	69.2	30.8	0.44	0.66	0.08		0.04		
CN–S	100	0	75.0	25.0	0.33	0.67	0.02			/	
CN–P	100	0	82.7	17.3	0.41	0.71	0.09				0.01
Au/CN	53.5	46.5	79.2	20.8		0.68	0.02	0.003			
Au/CN–S	71.6	28.4	75.1	24.9		0.68	0.03	0.003			

Looking at the C/N surface atomic ratios (Table 3), they are close to 0.67, whatever the bare or doped g-C_3N_4 material, and lower than the theoretical value of 0.75, suggesting a lower quality of polymerization and the presence of C-defective structures on the surface of the materials. However, the P-doped sample shows the highest C/N ratio, confirming better polymerization degree that may be correlated to better crystallinity as previously observed from XRD analyses.
Looking at B1s and P2p spectra (Fig. S2), the typical contributions at 191.9 eV and 133.2 eV, respectively, are observed and are characteristic of oxidized B and P species that might also explain the slightly larger O/C surface atomic ratios even if those contributions are too low to be distinguished from O1s spectra. Moreover, the two P2p3/2 and P2p1/2 cannot be distinguished, due to the low P2p peak intensity and low signal to noise ratio.
One can underline that B and P global wt.% contents, of 0.87% and 0.70% respectively, as determined from ICP analyses (Table 1), are much higher than the related B/C and P/C surface atomic ratios found by XPS (Table 3) (B/C and P/C at.% of 0.04 and 0.01 corresponding to 0.16 and 0.70 wt% of B and P, respectively).It suggests that the most important part (82 and 84%, respectively) of the dopant is incorporated inside the deeper porosity of g-C_3N_4.

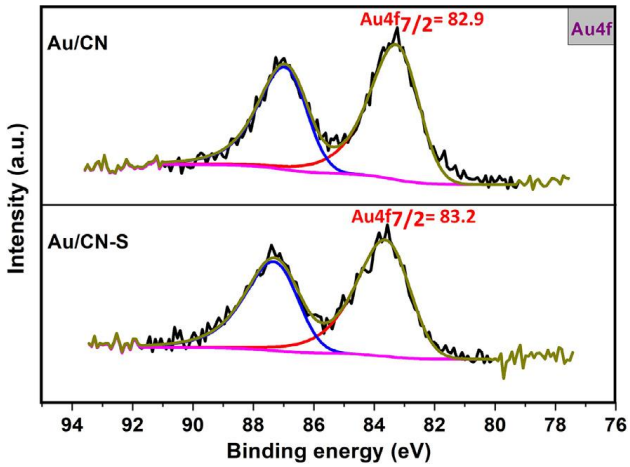

Fig. 5 *XPS spectra of Au4f.*

After Au deposition, XPS analyses of only the bare and S-doped g-C_3N_4 were performed (Fig. 5). From Au4f spectra, it can be observed that the Au4f7/2 component, expected at 84.0 eV in bulk gold, is shifted to lower binding energies, i.e. 82.9 eV and 83.2 eV in Au/CN and Au/S-CN, respectively. This has been observed before for SC-supported Au NPs [54]. It cannot be accounted for by the small size of Au NPs, since the related surface-core level shift effects would decrease binding energies by less than 0.4 eV [55]. Instead, the decrease in binding energies is attributed to a strong Au NPs-support interaction which allows for electron transfer from the support to Au NPs, resulting in negatively charged Au NPs [56].
Au/C surface ratios are found to be equal to ca. 0.3 at.% on both kinds of graphitic carbon nitride support (Table 3). This corresponds to approximatively 0.21 wt%, which is significantly lower than the global

weight percent of gold obtained by ICP analysis (Table 1). This indicates that a large part of Au NPs is located into the material deeper porosity.

TEM characterization

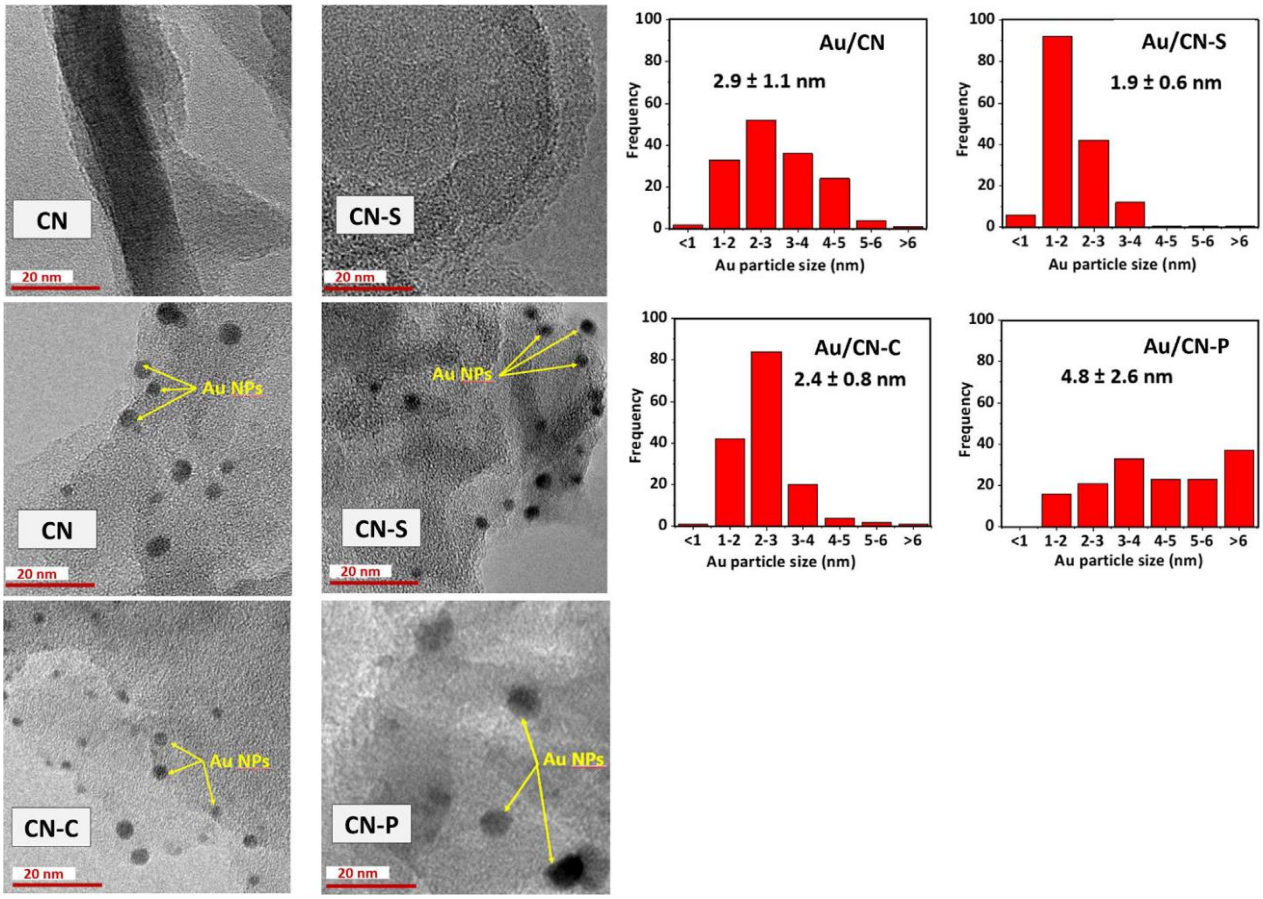

Fig. 6 *TEM micrographs of (Top-left) bare g-C_3N_4, (Top-right) CN-S, (Middle-left) Au/CN, (Middle-right) Au/CN-S, (Bottom Left) Au/CN-C and (Bottom Right) Au/CN-P nanostructures. Histograms showing Au NPs size distribution of Au/CN, Au/CN-S, Au/CN-C and Au/CN-P.*

From TEM images (Fig. 6-Top, example of bare and S-doped g-C_3N_4) one can clearly observe the typical lamellar structure of g-C_3N_4 with entangled nanosheets constituted of the stacking of ca. 10-15 layers, according to XRD analyses. Au NPs seem to be homogeneously deposited onto bare, S-doped and C-doped g-C_3N_4 support, their distributions in size following a monomodal tendency. However, Au NPs mean size and size distribution differ between bare S-doped and C-doped g-C_3N_4 (Fig. 6-Middle). Au NPs exhibit the smallestmean size (1.9 nm) onto S-doped g-C_3N_4, associated with the lowest standard deviation (0.6 nm), followed by C-doped g-C_3N_4 (2.4 nm with a standard deviation of 0.8 nm), compared to the larger mean size (2.9 nm) and broader deviation (1.1 nm) observed on bare g-C_3N_4. It must also be highlighted than P doping results in the largest Au NPs size (4.8 nm) broadly distributed without monomodal tendency. We assume that these features are related to different surface chemistries between depending on the dopant element. In particular, the higher amount of bridging-N atoms on C-doped and S-doped g-C_3N_4 may help to stabilize smaller Au particles, due to enhanced interaction between the gold precursor/gold seeds and the free electron doublet of such N atoms. Furthermore, interactions of Au NPs with S atoms could also contribute to the smallest size observed, due to the strong Au-S bond.

UV-vis absorption properties

From Fig. 7-Left, one can observe that doping leads to a displacement of the g-C_3N_4 absorption edge towards higher wavelengths, as confirmed by the determination of bang-gap value from Tauc plot (Fig.

S3) using Kubelka-Munk formula [57] (Table 2). The resulting band-gap values decrease from 2.85 eV on bare g-C_3N_4 to 2.80 eV, 2.75 eV, 2.70 eV and 2.50 eV respectively on P-doped, B-doped, S-doped and C-doped g-C_3N_4. Furthermore, it is worthy to underline that C-doping results in a very broad red-shift over the whole visible range allowing photons absorption still at 800 nm, while B-, P- and Sdoping exhibit more or less the same and much attenuated shift with absorption up to 500-550 nm. After deposition of a similar amount of gold (0.75 ± 0.04 wt%), the presence of Au NPs is evidenced by the characteristic SPR contribution centered at ca. 550 nm (Fig. 7-Right). The position of the SPR peak is not obviously affected by the nature of the g-C_3N_4 support. It is consistent with the similar size ranges of Au NPs produced on the different supports (2-6 nm) and their similar interactions with the support. However, the intensity of the SPR strongly depends on the C_3N_4 support. The largest intensity is obtained on the bare g-C_3N_4, while a much weaker intensity is observed on all doped materials. As the C-doped sample intrinsically shows high absorbance in the SPR region of Au NPs (Fig. 7-Left), it is not obvious to clearly identify the weak Au NPs SPR contribution, except considering a slight increase of the signal in the presence of Au NPs (Fig. 7-Right). The much weaker intensity of the SPR observed on the doped carbon nitrides cannot be due to much lower Au loadings, since these are all very similar (Table 1). However, a much larger population of Au NPs below 2 nm was found on CN-S, as compared with CN and with the other CN-X materials. Such small particles induce a significant enlargement/broadening of the SPR, which significantly limits its intensity [58]. Consequently, the difference in SPR peak intensity between bare and doped-gC_3N_4 may be related to differences in size distributions of Au NPs onto the various g-C_3N_4 supports. Inhibition of the surface accessibility of the smaller Au NPs, which may be buried in the deeper porosity of the less crystalline g-C_3N_4 supports, may also contribute to the weaker SPR signal [59].

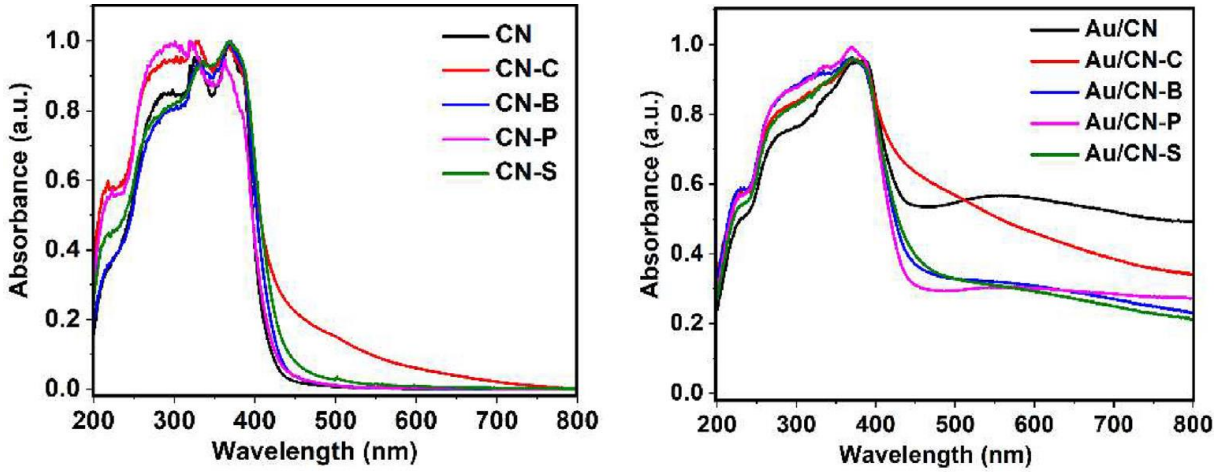

Fig. 7 *UV-Vis absorbance spectra of (left) bare and doped-g-C_3N_4 and of (right) Au/CN and Au/CN-X.*

Table 2 – Band-gap values, surface area, total pore volume and mean pore size diameter of bare and doped-gC_3N_4.

Sample	Eg (ev)	S_{BET} (m^2/g)	Vpore (cm^3/g)	Pore mean diameter (nm)
CN	2.83 ± 0.02	171 ± 2	0.94 ± 0.02	33
CN–C	2.50 ± 0.02	115 ± 3	0.56 ± 0.02	33
CN–B	2.77 ± 0.02	104 ± 2	0.54 ± 0.02	50
CN–P	2.79 ± 0.02	95 ± 2	0.50 ± 0.02	34
CN–S	2.70 ± 0.02	136 ± 1	0.62 ± 0.02	51

Photocatalytic performances and discussion

As it can be seen on Fig. 8-Top, the samples without Au deposition do not exhibit any observable photocatalytic activity towards H_2 production. Au deposition leads to H_2 production whatever the nature of g-C_3N_4 photocatalyst. As the gold content is the same on the different g-C_3N_4 based supports, it is

relevant to compare the photocatalytic activity of Au/g-C_3N_4 based photocatalysts. In the presence of gold, g-C_3N_4 doping results in enhancement of H_2 production, depending on the doping element. S-doping yields the highest activity increase, compared to bare g-C_3N_4 (270 µmol h^{-1} g^{-1}), reaching a hydrogen production of 608 µmol h^{-1} g^{-1}, followed by C-doping (532 µmol h^{-1} g^{-1}), by B-doping (376 µmol h^{-1} g^{-1}) and by P-doping which activity was close to that of the undoped material. Looking at cumulated H_2 production (Fig. 8-Bottom) on the most performant S-doped g-C_3N_4 material, it reaches ca. 347 µmol after 3 h under continuous irradiation. The corresponding recycling tests reveal a low relative loss of activity of ca. 6% after the first and second test, which only slightly increases after the third cycling test. This slight deactivation, already reported in literature [60] for g-C_3N_4-based photocatalysts, can be caused by degradation of TEOA under the experimental conditions used.

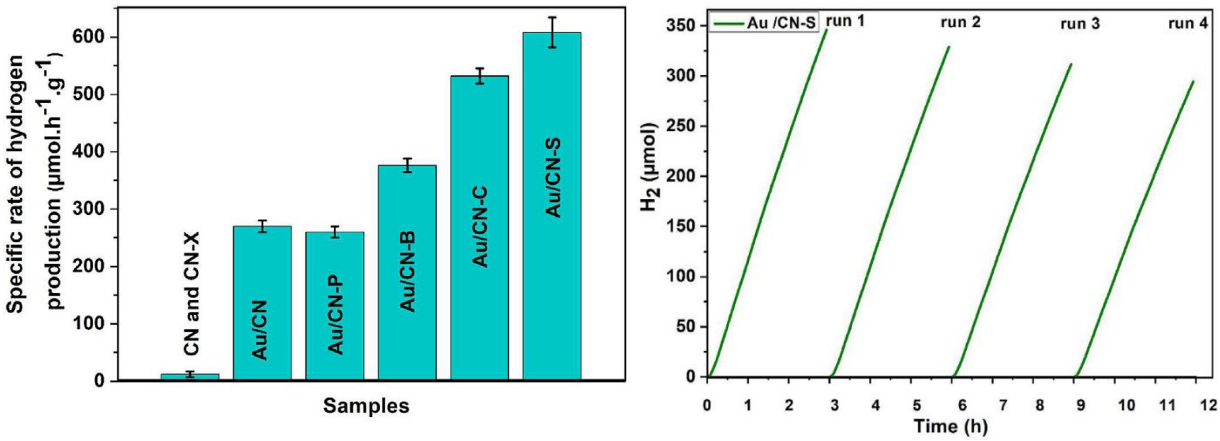

Fig. 8 *(Top) Specific rate of hydrogen production (µmol.h^{-1}.g^{-1}) under N_2 flow (100 mL min^{-1}) with 1 vol% TEOA as sacrificial agent. Relative experimental uncertainty of ca. 8%, (Bottom) Cumulative H_2 production - recycling tests on Au/CNeS sample.*

Presence of gold nanoparticles

The presence of gold nanoparticles in the semi-conductor is key in achieving these performances and to evaluate the impact of the SC doping on the photocatalytic activity. This can be attributed to the ability of Au NPs to act as electron traps, since the work function of gold (5.1-5.5 eV) is higher than the work function of C_3N_4 (4.3-4.7 eV) [61,62]. This is known to enhance photogenerated charge carrier separation, hence making their lifetime compatible with chemical reactions. In addition, Au NPs are known to act as co-catalysts in the production of hydrogen from water, enhancing in particular the final step, which consists in recombination of the reduced protons (Eq. (2)) [59].

$H_2O + 2h^+ \rightarrow ½\ O_2 + 2H^+$ (Eq. 1)
$2H^+ + 2e^- \rightarrow H_2$ (Eq. 2)

Localization of the dopant and impact on C_3N_4 structure and morphology

Even if the extent of doping and its impact on the semiconductor morphology and Au NPs size distribution is not the same depending on the nature of the non-metal dopant, one can observe that it results, in any case, in a more or less pronounced improvement of photocatalytic H_2 production under simulated solar light irradiation by modulating mainly the surface morphology, as well as electronic and optical properties, compared to bare g-C_3N_4. It has already been reported in literature that usually non-metal doping element introduction breaks the symmetry of g-C_3N_4 and thus results in faster separation of electron-hole pairs [63].

Furthermore, in addition to limitation of photoinduced electrons and holes recombination and prolonging the carrier lifetime, non-metal incorporation allows to harvest visible light absorption [64,65]. Over the past recent years, a lot of literature focusing on non-metal doping of g-C_3N_4 has been published [66,67]. Although there are many reports on nonmetal element doping, the detailed effect on band-gap and electronic structure are rarely reported. However, the real effects strongly depend on the nature of the dopant elements (C, S, P, B), on their content, on the doping element-containing precursor

used and more generally on the method of doping. From our results, no changes have been evidenced neither concerning the structural features of g-C_3N_4 in-plane assembly in terms of periodic arrangement of C and N atoms and of ordered assembly of aromatic s-triazine-based rings (XRD, TGA), nor by the presence of characteristic functional groups (FTIR). One must also highlight the absence of structural and surface modification after photocatalytic tests, according to FT-IR (Fig. S4), and to XRD spectra (Fig. S5).

The very low amount of doping elements considered in this study however does not allow us to fully exclude substitution of the atoms constituting the s-triazine-based units to form new in-plane bonds with the doping elements. Nevertheless, our study does show that doping can slightly impact the stacking of those structural units. Doping indeed leads to an increase of the size of tri-s-triazine units (XRD), probably due to incorporation of the doping elements into interplanar hollow spaces/cavities, resulting in a possible slight deformation, keeping in mind the respective size of S (180 p.m.), B (180 p.m.), P (195 p.m.), C (177 p.m.) and N (155 p.m.) ones. One can also mention that doping results in slightly increased interplanar stacking distance, probably due to the weakest Wan der Waals inter-layer interactions. Furthermore, XRD peak intensities decrease, suggesting that doping hinders g-C_3N_4 growth and thus leads to slightly smaller crystal thickness. More precisely, S- and B-doping exhibit the lowest number of stacked layers, and consequently the lowest crystallinity.

Our results clearly show that doping impacts the porosity of the material by decreasing the total surface area and pore volume (N_2 physisorption). P-doping yields the most important loss of accessible surface, and B-doping yields the lowest pore volume. Some literature also reports a lowering of surface area after doping, although a lot of studies mention an increase. Decrease in surface area can be explained by the introduction of non-metal elements into urea-condensation reaction, thus changing the texture and the surface morphology, such as collapse of mesopores [68]. Looking at the pore size distributions, one can clearly conclude that doping decreases essentially the pore volume associated with the inter-planar cavities. These results thus further support the presence of dopants in the inter-planar hollow space like some authors pointed out for B, F and P doping [68], which may explain why variations in the surface area and/or pore volume follow the order of the doping element size. Nevertheless, they do not exclude the possible incorporation of doping element inside intra-planar cavities of s-triazine aromatic rings.

From XPS results, interesting complementary information and assumptions can be deduced. The decrease in C/N surface atomic ratios resulting from S-, C- and B-doping suggests a lower quality of polymerization confirming lower quality of crystallization, except for P-doping (C/N value closer to the theoretical one), as confirmed by XRD analyses. Moreover, doping (with the exception of B- and P-doping) results in the relative increase in bridging-N (N-(C_3) groups) compared to graphitic-N (belonging to s-triazine units). This relative increase in bridging-N atoms compared to graphitic ones may be associated with the increase in interplanar hollow space and cavities revealed by porosity measurements. It suggests that the doping element is introduced in the large cavity of the intraplanar structures and mainly in stronger interaction with the bridging coordinated-N atoms. Unlike what has been observed in other XPS studies, there is no evidence for the replacement/incorporation of doping atoms, nor for the formation of new bonds into the planar framework of g-C_3N_4 [15,16,43,65], but again, this may be due to the very low amount of dopant incorporated.

Optical and electronic properties

It is well admitted in literature that non-metal doping is a good strategy to adjust electronic properties, considering that the doping element may be an atom in the replacement lattice, or existing in a planar cavity of g-C_3N_4, and that hybridization may happen between the doped orbital and molecular orbital of g-C_3N_4. Nevertheless, as far as we know, visible light harvesting was never observed to that extent. Band gap structure is one of the main factors for efficient photoexcitation. Generally, non-metal doping impacts the intrinsic electronic and band structure of g-C_3N_4 with obvious identification of absorption tailing peak in the range 450-600 nm. In our case, incorporation of doping elements inside the inter-planar hollow cavities may help for better electron delocalization and thus increased charge carrier spatial separation. Thus introducing doping atoms could tune the electron excitation, transfer and localization in g-C_3N_4 thus improving charge transfer and separation.

Structure/activity correlation

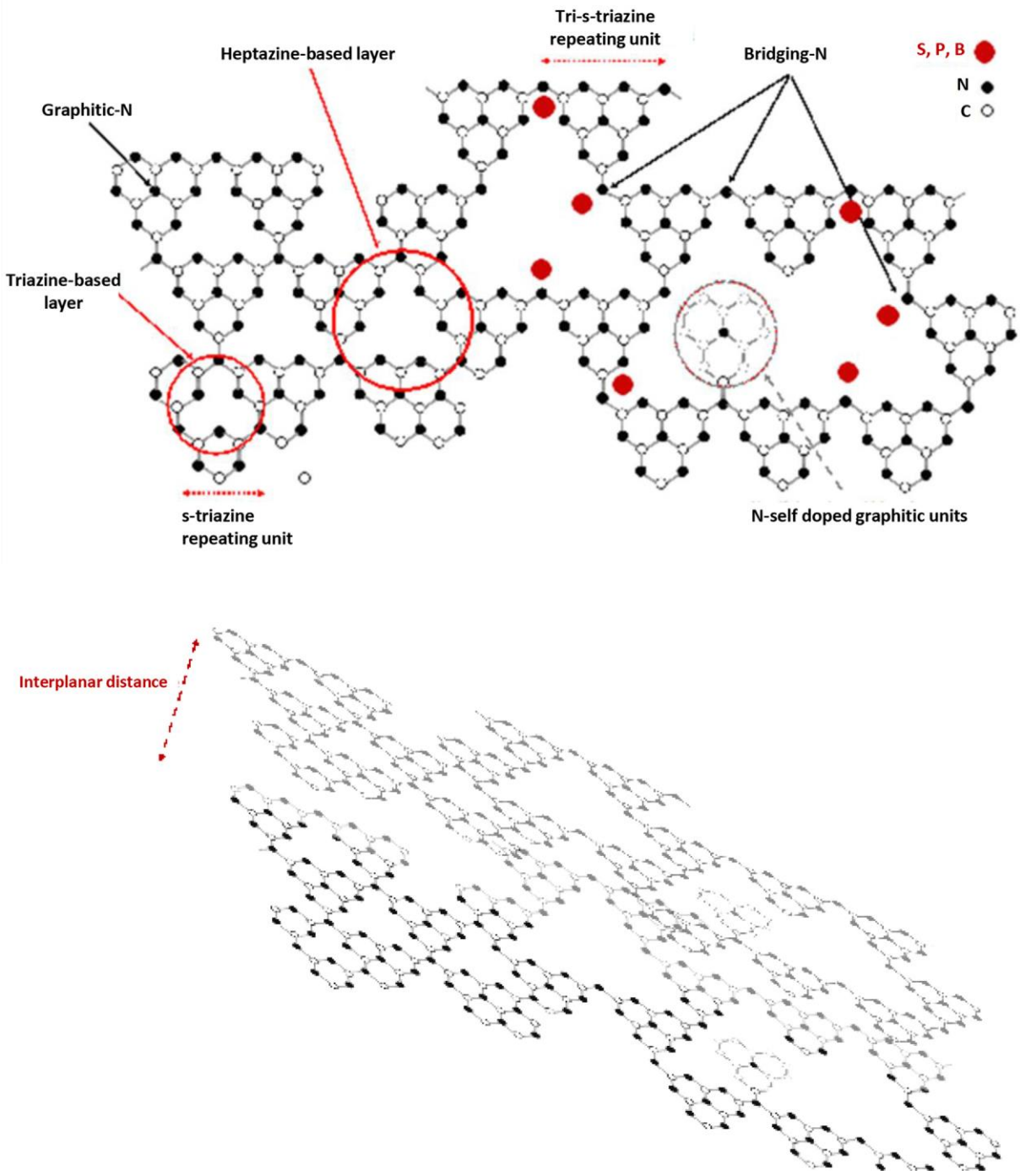

Fig. 9 *Scheme of (Top) doped-g-C_3N_4 layer, (Bottom) Interplanar hollow spheres/cavities resulting from stacking of successive layers.*

From all the aforementioned results, one may deduce that under our doping conditions, the doping elements are present at very low concentration, compared to other studies related to non-metal g-C_3N_4 doping, and appear to be mainly inserted into the large cavities of the interplanar hollow space in interaction with bridging-N atoms (Fig. 9), this interaction being stronger for C- and S-doping. In the case of P- and B-doping it is observed that these elements are oxidized in surface. This observation was not evidenced (due to too low concentrations) on C- and S-doped g-C_3N_4. Amongst the different doping elements studied here, they all resulted in improvement of artificial solar-light driven H_2 production from water in presence of low amount of sacrificial agent, but the benefit is more or less pronounced.
P-doping leads, after gold deposition, to almost no improved photocatalytic activity. One can recall that P-doped C_3N_4 exhibits the highest crystallinity, largest heptazine repeating motif size and lowest surface

area. Furthermore, as P element shows the largest unit size amongst all the doping elements studied, it may yield to some deformation and tiltangularity of the s-triazine unit assemblies, and thus limit optimal π-electron delocalization in g-C_3N_4 matrix system. One can also mention that P-doping also leads to an important surface area decrease and that Au/P-C_3N_4 contains the highest mean size of Au NPs, furthermore not homogeneously deposited onto the support. Furthermore, P doping is known to not significantly alter the work function of C_3N_4 [68].

C-doped C_3N_4 is one of the most performant material, leading to ca. two times more H_2 production compared to the bare reference sample. It has already been reported that citric acid-added urea synthesis for obtaining C-doped g-C_3N_4 results in the formation of few loaded N-doped graphitic carbon units in g-C3N4 matrix, but too small to be detected with certainty using ICP, XRD, Raman or XPS analyses [16]. In addition, in our case considering also that the C-doped sample exhibits the lowest N/C volumic ratio, one may also assume the presence of very small N-doped graphitic carbon inside the g-C_3N_4 matrix, issued from citric acid playing the role of C-source and reacting with urea by copolymerization during the process of g-C_3N_4 synthesis. Carboxylic groups of citric acid may react with amine groups of urea and the resulting copolymerized species incorporated in g-C_3N_4 matrix. However, in our case, due to the low concentration of citric acid added without changing the planar triazine molecular structure, it is hard to distinguish different marked features between C-doped and bare g-C_3N_4 based on our characterizations. One of the most relevant consequence of C-doping is the remarkable visible light harvesting ability, extending the absorption to the whole visible light region, probably as a result of enhanced electron delocalization onto some N-doped graphitic carbon units. This extended light absorption in the visible range may allow, in the Au/C-C_3N_4 photocatalyst, for field-enhancement effects, as Au NPs also absorb in the visible range and are therefore able to act as antennas [69]. This effect results in an increased number of photogenerated charge carriers within the semiconductor, which may contribute to the enhanced photocatalytic activity observed over Au/C-C_3N_4. Hydrogen production may be further enhanced by the small size of Au NPs. The higher metallic dispersion indeed exposes a higher number of catalytically active sites for proton recombination and also a higher frequency of the most active, lowcoordinated surface atoms [70]. The smaller size of Au NPs obtained at the same loading than the other photocatalysts also implies a higher number of Au NPs on the semi-conductor and a larger interfacial perimeter between Au NPs and C-g-C_3N_4, which may also favor the proton recombination step by increasing the occurrence of H migration to Au NPs via reverse spillover over the C-g-C_3N_4 surface [71,72].

S-doped g-C_3N_4 photocatalyst exhibits the best H_2 production rate, more than 2.5 times higher compared to the undoped material. Unlike what has mostly been reported in literature [15,43,65] under our experimental doping conditions via thermal polymerization of urea and 2-thiobarbituric acid at low dosage, neither S atoms substituting N atoms in the aromatic ring of g-C_3N_4, nor formation of S=O or C-S bonds have been evidenced, although N/C volumic ratio reveals a slightly C-rich structure. Incorporation of S element into the inter-planar cavities, as already assumed previously, considering its Lewis acid properties may lower van der Waals interactions between stacked layers, decreases crystallinity, and increases the mesoporous/macroporous surface. S-doping exhibits the highest surface area amongst all the doped materials, followed by C-doping, which might be correlated with the two best photocatalytic performances. It must also be underlined that S-doping allows to keep a relatively important total pore volume, knowing that the other doping elements lead to a more important decrease compared to bare g-C_3N_4. We may assume that the very low S content may hinder pores collapse during urea condensation reaction. Furthermore, it must be mentioned that S atoms can act as Lewis acid sites, helping for better H_2O molecules adsorption. It has also been mentioned in literature [28] that S-doped graphitic carbon nitride may result in a more negative reduction potential, thus enhancing H_2 production. In addition, it is also admitted from PL, EIS and transient photocurrent measurements that S doping yields to the formation of more photogenerated electrons, to increased charge transfer and thus to lower recombination probability. S-doping is also known to yield a significant decrease in the work function of the parent g-C_3N_4, so that the electron trap effect and charge carrier lifetime enhancement upon Schottky contact with Au NPs would be significantly enhanced as compared with bare Au/g-C_3N_4. Moreover, low size Au NPs have been observed on S-doped C_3N_4. This may further enhance electron-trapping properties, due to the increase in the work function of gold in small Au NPs [73], but also via the higher number of Au NPs (similar loading) and thus the higher number of Au/S-g-C_3N_4 interfaces. Finally, the low Au NPs size also enhances the cocatalytic activity of Au for H_2 formation from proton

recombination via the higher metallic dispersion, the higher number of Au/S-g-C_3N_4 interfaces and the frequency of the highly active, low-coordinated surface atoms.

Conclusion

Generally, photocatalytic activity of g-C_3N_4 is not satisfactory because of limitations such as relatively low visible light absorbance, poor specific surface area, and rapid recombination of photogenerated electron-hole pairs. In this paper we optimized a one pot strategy for non-metal doping of g-C_3N_4 by incorporating a very low dosage of doping element precursors into urea before thermal polycondensation, which allowed us to overcome those limitations. The resulting doped g-C_3N_4 materials retain the original framework of g-C_3N_4 and high surface area by hindering pore collapse, especially in the case of C- and S-doped g-C_3N_4. Those photocatalysts exhibit enhanced visible light harvesting properties and suitable surfaces for the deposition and stabilization of small Au NPs, which are known to enhance charge separation of photogenerated electron-hole pairs. As a result, artificial solar light-driven H_2 production from H_2O, in the presence of low amount of TEOA as sacrificial agent, was enhanced by up to 100%.

Despite the very low level of doping and the uncertainty on the dopant location within the structure, successful doping of CN materials was achieved. In particular, Au/CN-S, which contains the lowest level of doping (0.03 wt%), yields the best activity (608 μmol/h/g), which is 2.3 times higher than bare Au/CN (270 μmol/h/g) and 1.5 times higher than the second-best doping material Au/CN-C (538 μmol/h/g). Au/CN-S is thus found to exhibit the most efficient combination of low stacking degree, high surface area, large mesoporosity, small Au NPs size and narrow Au NP size distribution to promote visible light harvesting, charge carrier separation and utilization, and ultimately H_2 formation. The low level of doping makes the investigation of the location of the dopant quite tricky and would require advanced characterization techniques.

Declaration of competing interest

The authors declare that they have no known competing financial interests or personal relationships that could have appeared to influence the work reported in this paper.

Acknowledgments

The authors are grateful to Centre islamique d'orientation et de l'enseignement supérieur (CIOES) for the PhD fellowship of Leila Hammoud. D. Ihiawakrim (UMR CNRS 7504) is thanked for acquiring TEM images. Dr. V. Papaefthimiou (UMR CNRS 7515) is thanked for acquiring XPS data.

Supplementary data

Supplementary data to this article can be found online at https://doi.org/10.1016/j.ijhydene.2023.03.284.

References

[1] Lewis NS, Nocera DG. Powering the planet: chemical challenges in solar energy utilization. Proc Natl Acad Sci USA 2006;103:15729-35. https://doi.org/10.1073/pnas.0603395103.

[2] Dou H, Long D, Zheng S, Zhang Y. A facile approach to synthesize graphitic carbon nitride microwires for enhanced photocatalytic H2 evolution from water splitting under full solar spectrum. Catal Sci Technol 2018;8:3599-609. https://doi.org/10.1039/C8CY00904J.

[3] Li X, Yu J, Low J, Fang Y, Xiao J, Chen X. Engineering heterogeneous semiconductors for solar water splitting. J Mater Chem 2015;3:2485-534. https://doi.org/10.1039/C4TA04461D.

[4] Marchal C. Synthèse et réactivité de nanocomposites Au/g-C3N4/TiO2 pour la production d'hydrogène par procédé photocatalytique sous illumination solaire et visible. University of Strasbourg; 2017.

[5] Bie C, Wang L, Yu J. Challenges for photocatalytic overall water splitting. Chem 2022;8:1567-74. https://doi.org/10.1016/j.chempr.2022.04.013.

[6] Rajeshwar K, Mcconnell R, Licht S. Solar hydrogen generation: toward a renewable energy future. 2008. https://doi.org/10.1007/978-0-387-72810-0.

[7] Fujishima A, Honda K. Electrochemical photolysis of water at a semiconductor electrode. Nature 1972;238:37-8. https://doi.org/10.1038/238037a0.

[8] Song X, Yang Q, Jiang X, Yin M, Zhou L. Porous graphitic carbon nitride nanosheets prepared under self-producing atmosphere for highly improved photocatalytic activity. Appl Catal B Environ 2017;217:322-30. https://doi.org/10.1016/j.apcatb.2017.05.084.
[9] Acharya L, Swain G, Mishra BP, Acharya R, Parida K. Development of MgIn2S4 microflower-embedded exfoliated B-doped g-C3N4 nanosheets: p-n heterojunction photocatalysts toward photocatalytic water reduction and H2O2 production under visible-light irradiation. ACS Appl Energy Mater 2022;5:2838-52. https://doi.org/10.1021/acsaem.1c03525.
[10] Mishra A, Mehta A, Basu S, Shetti NP, Reddy KR, Aminabhavi TM. Graphitic carbon nitride (g-C3N4)-based metal-free photocatalysts for water splitting: a review. Carbon 2019;149:693-721. https://doi.org/10.1016/j.carbon.2019.04.104.
[11] Rattan Paul D, Nehra SP. Graphitic carbon nitride: a sustainable photocatalyst for organic pollutant degradation and antibacterial applications. Environ Sci Pollut Res Int 2021;28:3888-96. https://doi.org/10.1007/s11356-020-09432-6.
[12] Zhou C, Liang Y, Xia W, Almatrafi E, Song B, Wang Z, et al. Single atom Mn anchored on N-doped porous carbon derived from spirulina for catalyzed peroxymonosulfate to degradation of emerging organic pollutants. J Hazard Mater 2023;441:129871. https://doi.org/10.1016/j.jhazmat.2022.129871.
[13] Zhou C, Almatrafi E, Tang X, Shao B, Xia W, Song B, et al. Investigation on the structure-performance of phthalic acid carboxyl position and carbon nitride towards efficient photocatalytic degradation of organic pollutants. Sep Purif Technol 2022;286:120464. https://doi.org/10.1016/j.seppur.2022.120464.
[14] Qin J, Wang S, Ren H, Hou Y, Wang X. Photocatalytic reduction of CO2 by graphitic carbon nitride polymers derived from urea and barbituric acid. Appl Catal B Environ 2015;179:1-8. https://doi.org/10.1016/j.apcatb.2015.05.005.
[15] Starukh H, Praus P. Doping of graphitic carbon nitride with non-metal elements and its applications in photocatalysis. Catalysts 2020;10:1119. https://doi.org/10.3390/catal10101119.
[16] Zhou Y, Zhang L, Huang W, Kong Q, Fan X, Wang M, et al. Ndoped graphitic carbon-incorporated g-C3N4 for remarkably enhanced photocatalytic H2 evolution under visible light. Carbon 2016;99:111-7. https://doi.org/10.1016/j.carbon.2015.12.008.
[17] Dong F, Wang Z, Sun Y, Ho W-K, Zhang H. Engineering the nanoarchitecture and texture of polymeric carbon nitride semiconductor for enhanced visible light photocatalytic activity. J Colloid Interface Sci 2013;401:70-9. https://doi.org/10.1016/j.jcis.2013.03.034.
[18] Zhao Z, Ma Y, Fan J, Xue Y, Chang H, Masubuchi Y, et al. Synthesis of graphitic carbon nitride from different precursors by fractional thermal polymerization method and their visible light induced photocatalytic activities. J Alloys Compd 2018;735:1297-305. https://doi.org/10.1016/j.jallcom.2017.11.033.
[19] Holst JR, Gillan EG. From triazines to heptazines: deciphering the local structure of amorphous nitrogen-rich carbon nitride materials. J Am Chem Soc 2008;130:7373-9. https://doi.org/10.1021/ja709992s.
[20] Xu B, Ahmed MB, Zhou JL, Altaee A, Xu G, Wu M. Graphitic carbon nitride based nanocomposites for the photocatalysis of organic contaminants under visible irradiation: progress, limitations and future directions. Sci Total Environ 2018;633:546-59. https://doi.org/10.1016/j.scitotenv.2018.03.206.
[21] Yu J, Wang S, Low J, Xiao W. Enhanced photocatalytic performance of direct Z-scheme g-C3N4-TiO2 photocatalysts for the decomposition of formaldehyde in air. Phys Chem Chem Phys 2013;15:16883-90. https://doi.org/10.1039/C3CP53131G.
[22] Mishra BP, Parida K. Orienting Z scheme charge transfer in graphitic carbon nitride-based systems for photocatalytic energy and environmental applications. J Mater Chem 2021;9:10039-80. https://doi.org/10.1039/D1TA00704A.
[23] He C, Xia W, Zhou C, Huang D, Zhang C, Song B, et al. Rational design to manganese and oxygen co-doped polymeric carbon nitride for efficient nonradical activation of peroxymonosulfate and the mechanism insight. Chem Eng J 2022;430:132751. https://doi.org/10.1016/j.cej.2021.132751.
[24] Mishra BP, Acharya L, Subudhi S, Parida K. Oxygen vacancy rich α-MnO2@B/O-g-C3N4 photocatalyst: a thriving 1D-2D surface interaction effective towards photocatalytic O2 and H2 evolution through Z-scheme charge dynamics. Int J Hydrogen Energy 2022;47:32107-20. https://doi.org/10.1016/j.ijhydene.2022.07.125.
[25] Xu J, Zhang L, Shi R, Zhu Y. Chemical exfoliation of graphitic carbon nitride for efficient heterogeneous photocatalysis. J Mater Chem 2013;1:14766-72. https://doi.org/10.1039/C3TA13188B.
[26] Yan J, Zhou C, Li P, Chen B, Zhang S, Dong X, et al. Nitrogenrich graphitic carbon nitride: controllable nanosheet-like morphology, enhanced visible light absorption and superior photocatalytic performance. Colloids Surf A Physicochem Eng Asp 2016;508. https://doi.org/10.1016/j.colsurfa.2016.08.067.
[27] Wang F, Lei W, Pan X, Ye Z. Facile synthesis of graphitic carbon nitride via copolymerization of melamine and TCNQ for photocatalytic hydrogen evolution. Nanotechnology 2020;31:475406. https://doi.org/10.1088/1361-6528/ab9ed7.

[28] Long D, Wang L, Cai H, Rao X, Zhang Y. Sulfur doped carbonrich g-C3N4 for enhanced photocatalytic H2 evolution: morphology and crystallinity effect. Catal Lett 2020;150:2487-96. https://doi.org/10.1007/s10562-020-03156-5.
[29] Zhang S, Hu C, Ji H, Zhang L, Li F. Facile synthesis of nitrogen-deficient mesoporous graphitic carbon nitride for highly efficient photocatalytic performance. Appl Surf Sci 2019;478:304-12. https://doi.org/10.1016/j.apsusc.2019.01.270.
[30] Cao J, Fan H, Wang C, Ma J, Dong G, Zhang M. Facile synthesis of carbon self-doped g-C3N4 for enhanced photocatalytic hydrogen evolution. Ceram Int 2020;46:7888-95. https://doi.org/10.1016/j.ceramint.2019.12.008.
[31] Wang Y, Cai H, Qian F, Li Y, Yu J, Yang X, et al. Facile one-step synthesis of onion-like carbon modified ultrathin g-C3N4 2D nanosheets with enhanced visible-light photocatalytic performance. J Colloid Interface Sci 2019;533:47-58. https://doi.org/10.1016/j.jcis.2018.08.039.
[32] Acharya L, Nayak S, Pattnaik SP, Acharya R, Parida K. Resurrection of boron nitride in p-n type-II boron nitride/B-doped-g-C3N4 nanocomposite during solid-state Z-scheme charge transfer path for the degradation of tetracycline hydrochloride. J Colloid Interface Sci 2020;566:211-23. https://doi.org/10.1016/j.jcis.2020.01.074.
[33] Mishra BP, Biswal L, Das S, Acharya L, Parida K. Architecture and kinetic studies of photocatalytic H2O2 generation and H2 evolution through regulation of spatial charge transfer via Z-scheme path over a (001) facet engineered TiO2@MXene/Bg-C3N4 ternary hybrid. Langmuir 2023;39:957-71. https://doi.org/10.1021/acs.langmuir.2c02315.
[34] Yu H, Jiang X, Shao Z, Feng J, Yang X, Liu Y. Metal-free halfmetallicity in B-doped gh-C3N4 systems. Nanoscale Res Lett 2018;13:57. https://doi.org/10.1186/s11671-018-2473-x.
[35] Wang Z, Chen M, Huang Y, Shi X, Zhang Y, Huang T, et al. Self-assembly synthesis of boron-doped graphitic carbon nitride hollow tubes for enhanced photocatalytic NOx removal under visible light. Appl Catal B Environ 2018;239:352-61. https://doi.org/10.1016/j.apcatb.2018.08.030.
[36] Gao D, Liu Y, Liu P, Si M, Xue D. Atomically thin B doped g-C3N4 nanosheets: high-temperature ferromagnetism and calculated half-metallicity. Sci Rep 2016;6:35768. https://doi.org/10.1038/srep35768.
[37] Li X, Zhu P, Liu C, Pang H. One step synthesis of boron-doped carbon nitride derived from 4-pyridylboronic acid as biosensing platforms for assessment of food safety. Chem Commun 2019;55:9160-3. https://doi.org/10.1039/C9CC03787J.
[38] Su C, Zhou Y, Zhang L, Yu X, Gao S, Sun X, et al. Enhanced n/p* electron transition of porous P-doped g-C3N4 nanosheets for improved photocatalytic H2 evolution performance. Ceram Int 2020;46:8444-51. https://doi.org/10.1016/j.ceramint.2019.12.079.
[39] Zhou Y, Zhang L, Liu J, Fan X, Wang B, Wang M, et al. Brand new P-doped g-C3N4: enhanced photocatalytic activity for H2 evolution and Rhodamine B degradation under visible light. J Mater Chem 2015;3:3862-7. https://doi.org/10.1039/C4TA05292G.
[40] Guo S, Tang Y, Xie Y, Tian C, Feng Q, Zhou W, et al. P-doped tubular g-C3N4 with surface carbon defects: universal synthesis and enhanced visible-light photocatalytic hydrogen production. Appl Catal B Environ 2017;218:664-71. https://doi.org/10.1016/j.apcatb.2017.07.022.
[41] Liu G, Niu P, Sun C, Smith SC, Chen Z, Lu GQ (Max), et al. Unique electronic structure induced high photoreactivity of sulfur-doped graphitic C3N4. J Am Chem Soc 2010;132:11642-8. https://doi.org/10.1021/ja103798k.
[42] Sakthivel A, Chandrasekaran A, Jayakumar S, Manickam P, Alwarappan S. Sulphur doped graphitic carbon nitride as an efficient electrochemical platform for the detection of acetaminophen. J Electrochem Soc 2019;166:B1461. https://doi.org/10.1149/2.0021915jes.
[43] Qin H, Lv W, Bai J, Zhou Y, Wen Y, He Q, et al. Sulfur-doped porous graphitic carbon nitride heterojunction hybrids for enhanced photocatalytic H2 evolution. J Mater Sci 2019;54:4811-20. https://doi.org/10.1007/s10853-018-3168-5.
[44] Xie L, Dai Y, Zhou Y, Chang X, Yin L. Sulfur (VI) modified graphite carbon nitride nanosheets with chrysanthemum-like structure and enhanced photocatalytic activity. Chem Phys Lett 2018;693:1-7. https://doi.org/10.1016/j.cplett.2017.12.071.
[45] Li Y, Wang S, Chang W, Zhang L, Wu Z, Song S, et al. Preparation and enhanced photocatalytic performance of sulfur doped terminal-methylated g-C3N4 nanosheets with extended visible-light response. J Mater Chem 2019;7:20640-8. https://doi.org/10.1039/C9TA07014A.
[46] Lv H, Huang Y, Koodali RT, Liu G, Zeng Y, Meng Q, et al. Synthesis of sulfur-doped 2D graphitic carbon nitride nanosheets for efficient photocatalytic degradation of phenol and hydrogen evolution. ACS Appl Mater Interfaces 2020;12:12656-67. https://doi.org/10.1021/acsami.9b19057.
[47] Yuan S, Cui P, Zhang Y, Zhang H, Huo L, Gao Y. Popping of g- C3N4 mixed with cupric nitrate: facile synthesis of Cu-based catalyst for construction of C N bond. Green Energy Environ 2018;3. https://doi.org/10.1016/j.gee.2018.08.003.

[48] Gao J, Zhou Y, Li Z, Yan S, Wang N, Zou Z. High-yield synthesis of millimetre-long, semiconducting carbon nitride nanotubes with intense photoluminescence emission and reproducible photoconductivity. Nanoscale 2012;4:3687-92. https://doi.org/10.1039/C2NR30777D.
[49] Ong W-J, Tan L-L, Ng YH, Yong S-T, Chai S-P. Graphitic carbon nitride (g-C3N4)-based photocatalysts for artificial photosynthesis and environmental remediation: are we a step closer to achieving sustainability? Chem Rev 2016;116:7159-329. https://doi.org/10.1021/acs.chemrev.6b00075.
[50] Jimenez-Calvo P, Caps V, Ghazzal MN, Colbeau-Justin C, Keller V. Au/TiO2(P25)-gC3N4 composites with low gC3N4 content enhance TiO2 sensitization for remarkable H2 production from water under visible-light irradiation. Nano Energy 2020;75:104888. https://doi.org/10.1016/j.nanoen.2020.104888.
[51] Papailias I, Giannakopoulou T, Todorova N, Demotikali D, Vaimakis T, Trapalis C. Effect of processing temperature on structure and photocatalytic properties of g-C3N4. Appl Surf Sci 2015;358:278-86. https://doi.org/10.1016/
j.apsusc.2015.08.097.
[52] Cao S, Low J, Yu J, Jaroniec M. Polymeric photocatalysts based on graphitic carbon nitride. Adv Mater 2015;27:2150-76. https://doi.org/10.1002/adma.201500033.
[53] Ong W-J, Putri LK, Tan L-L, Chai S-P, Yong S-T. Heterostructured AgX/g-C3N4 (X=Cl and Br) nanocomposites via a sonication-assisted deposition-precipitation approach: emerging role of halide ions in the synergistic photocatalytic reduction of carbon dioxide. Appl Catal B Environ 2016;180:530-43. https://doi.org/10.1016/j.apcatb.2015.06.053.
[54] Lignier P, Comotti M, Schüth F, Rousset J-L, Caps V. Effect of the titania morphology on the Au/TiO2-catalyzed aerobic epoxidation of stilbene. Catal Today 2009;141:355-60. https://doi.org/10.1016/j.cattod.2008.04.032.
[55] Citrin PH, Wertheim GK, Baer Y. Core-level binding energy and density of states from the surface atoms of gold. Phys Rev Lett 1978;41:1425-8. https://doi.org/10.1103/PhysRevLett.41.1425.
[56] Radnik J, Mohr C, Claus P. On the origin of binding energy shifts of core levels of supported gold nanoparticles and dependence of pretreatment and material synthesis. Phys Chem Chem Phys 2003;5:172-7. https://doi.org/10.1039/B207290D.
[57] Acharya L, Pattnaik SP, Behera A, Acharya R, Parida K. Exfoliated boron nitride (e-BN) tailored exfoliated graphitic carbon nitride (e-CN): an improved visible light mediated photocatalytic approach towards TCH degradation and H2 evolution. Inorg Chem 2021;60:5021-33. https://doi.org/10.1021/acs.inorgchem.1c00062.
[58] Caux M, Menard H, AlSalik Y M, Irvine Jt S, Idriss H. Photocatalytic hydrogen production over Au/g-C3N4 : effect of gold particle dispersion and morphology. Phys Chem Chem Phys 2019;21:15974-87. https://doi.org/10.1039/C9CP02241D.
[59] Marchal C, Piquet A, Behr M, Cottineau T, Papaefthimiou V, Keller V, et al. Activation of solid grinding-derived Au/TiO2 photocatalysts for solar H2 production from water-methanol mixtures with low alcohol content. J Catal 2017;352:22-34. https://doi.org/10.1016/j.jcat.2017.04.035.
[60] Marchal C, Cottineau T, Mendez-Medrano MG, Colbeau-Justin C, Caps V, Keller V. Au/TiO2-gC3N4 nanocomposites for enhanced photocatalytic H2 production from water under visible light irradiation with very low quantities of sacrificial agents. Adv Energy Mater 2018;8:1702142. https://doi.org/10.1002/aenm.201702142.
[61] Zhu B, Tan H, Fan J, Cheng B, Yu J, Ho W. Tuning the strength of built-in electric field in 2D/2D g-C3N4/SnS2 and g-C3N4/ZrS2 S-scheme heterojunctions by nonmetal doping. J Materiomics 2021;7:988-97. https://doi.org/10.1016/j.jmat.2021.02.015.
[62] Zhu B, Zhang J, Jiang C, Cheng B, Yu J. First principle investigation of halogen-doped monolayer g-C3N4 photocatalyst. Appl Catal B Environ 2017;207:27-34. https://doi.org/10.1016/j.apcatb.2017.02.020.
[63] Huang Z-F, Song J, Pan L, Wang Z, Zhang X, Zou J-J, et al. Carbon nitride with simultaneous porous network and Odoping for efficient solar-energy-driven hydrogen evolution. Nano Energy 2015;12:646-56. https://doi.org/10.1016/j.nanoen.2015.01.043.
[64] Starukh H, Praus P. Doping of graphitic carbon nitride with non-metal elements and its applications in photocatalysis. Catalysts 2020;10:1119. https://doi.org/10.3390/catal10101119.
[65] Zheng Y, Liu Y, Guo X, Chen Z, Zhang W, Wang Y, et al. Sulfur-doped g-C3N4/rGO porous nanosheets for highly efficient photocatalytic degradation of refractory contaminants. J Mater Sci Technol 2020;41:117-26. https://doi.org/10.1016/j.jmst.2019.09.018.
[66] Hasija V, Raizada P, Sudhaik A, Sharma K, Kumar A, Singh P, et al. Recent advances in noble metal free doped graphitic carbon nitride based nanohybrids for photocatalysis of organic contaminants in water: a review. Appl Mater Today 2019;15:494-524. https://doi.org/10.1016/j.apmt.2019.04.003.
[67] Jiang L, Yuan X, Pan Y, Liang J, Zeng G, Wu Z, et al. Doping of graphitic carbon nitride for photocatalysis: a review. ApplCatal B Environ 2017;217:388-406. https://doi.org/10.1016/j.apcatb.2017.06.003.
[68] Luo Y, Wang J, Yu S, Cao Y, Ma K, Pu Y, et al. Nonmetal element doped g-C3N4 with enhanced H2 evolution under visible light irradiation. J Mater Res 2018;33:1268-78. https://doi.org/10.1557/jmr.2017.472.

[69] Gellé A, Jin T, de la Garza L, Price GD, Besteiro LV, Moores A. Applications of plasmon-enhanced nanocatalysis to organic transformations. Chem Rev 2020;120:986-1041. https://doi.org/10.1021/acs.chemrev.9b00187.
[70] Vigneron F, Caps V. Evolution in the chemical making of gold oxidation catalysts. Compt Rendus Chem 2016;19:192-8. https://doi.org/10.1016/j.crci.2015.11.015.
[71] Luna AL, Novoseltceva E, Louarn E, Beaunier P, Kowalska E, Ohtani B, et al. Synergetic effect of Ni and Au nanoparticles synthesized on titania particles for efficient photocatalytic hydrogen production. Appl Catal B Environ 2016;191:18-28. https://doi.org/10.1016/j.apcatb.2016.03.008.
[72] Mendez-Medrano MG, Kowalska E, Lehoux A, Herissan A, Ohtani B, Rau S, et al. Surface modification of TiO2 with Au nanoclusters for efficient water treatment and hydrogen generation under visible light. J Phys Chem C 2016;120:25010-22. https://doi.org/10.1021/acs.jpcc.6b06854.
[73] Zhang Y, Pluchery O, Caillard L, Lamic-Humblot A-F, Casale S, Chabal YJ, et al. Sensing the charge state of single gold nanoparticles via work function measurements. Nano Lett 2015;15:51-5. https://doi.org/10.1021/nl503782s.